Ionised outflows in $z \sim 2.4$ quasar host galaxies [*]

S. Carniani[1, 2, 3, 4], A. Marconi[1, 2], R. Maiolino[3, 4], B. Balmaverde[2], M. Brusa[5, 6], M. Cano-Díaz[7] C. Cicone[3, 4, 8], A. Comastri[6], G. Cresci[1, 2], F. Fiore[9], C. Feruglio[9, 10, 11], F. La Franca[12], V. Mainieri[13], F. Mannucci[2], T. Nagao[14], H. Netzer[15], E. Piconcelli[9], G. Risaliti[2], R. Schneider[9], O. Shemmer[16]

[1] Dipartimento di Fisica e Astronomia, Università di Firenze, Via G. Sansone 1, I-50019, Sesto Fiorentino (Firenze), Italy
[2] INAF - Osservatorio Astrofisico di Arcetri, Largo E. Fermi 5, I-50125, Firenze, Italy
[3] Cavendish Laboratory, University of Cambridge, 19 J. J. Thomson Ave., Cambridge CB3 0HE, UK
[4] Kavli Institute for Cosmology, University of Cambridge, Madingley Road, Cambridge CB3 0HA, UK
[5] Dipartimento di Fisica e Astronomia, Università di Bologna, viale Berti Pichat 6/2, 40127 Bologna, Italy
[6] INAF - Osservatorio Astronomico di Bologna, via Ranzani 1, 40127 Bologna, Italy
[7] Instituto de Astronomía - UNAM, Mexico City, Mexico
[8] Institute for Astronomy, Department of Physics, ETH Zurich, Wolfgang-Pauli-Strasse 27, CH-8093 Zurich, Switzerland
[9] INAF - Osservatorio Astronomico di Roma, via Frascati 33, 00040 Monteporzio Catone, Italy
[10] Scuola Normale Superiore, Piazza dei Cavalieri 7, 56126 Pisa, Italy
[11] IRAM - Institut de Radio Astronomie Millimétrique, 300 rue de la Piscine, 38406 Saint Martin d'Hères, France
[12] Dipartimento di Matematica e Fisica, Università Roma Tre, via della Vasca Navale 84, I-00146 Roma, Italy
[13] European Southern Observatory, Karl-Schwarzschild-str. 2, 85748 Garching bei München, Germany
[14] Research Center for Space and Cosmic Evolution, Ehime University, Bunkyo-cho 2-5, Matsuyama, 790-8577 Ehime, Japan
[15] School of Physics and Astronomy, The Sackler Faculty of Exact Sciences, Tel-Aviv University, Tel-Aviv 69978, Israel
[16] Department of Physics, University of North Texas, Denton, TX 76203, USA

June 11, 2015

ABSTRACT

Aims. AGN-driven outflows are invoked by galaxy evolutionary models to quench star formation and to explain the origin of the relations observed locally between super massive black holes and their host galaxies. This work aims to detect the presence of extended ionised outflows in luminous quasars where we expect the maximum activity both in star formation and in black hole accretion. Currently, there are only a few studies based on spatially resolved observations of outflows at high redshift, $z > 2$.
Methods. We analyse a sample of six luminous ($L > 10^{47}$ erg/s) quasars at $z \sim 2.4$, observed in H-band using the near-IR integral field spectrometer SINFONI at VLT. We perform a kinematic analysis of the [OIII] emission line at $\lambda = 5007$Å.
Results. We detect fast, spatially extended outflows in five out of six targets. [OIII]$\lambda5007$ has a complex gas kinematic, with blue-shifted velocities of a few hundreds of km/s and line widths up to 1500 km/s. Using the spectroastrometric method we infer size of the ionised outflows of up to ~2 kpc. The properties of the ionised outflows, mass outflow rate, momentum rate and kinetic power, are correlated with the AGN luminosity. The increase in outflow rate with increasing AGN luminosity is consistent with the idea that a luminous AGN pushes away the surrounding gas through fast outflows driven by radiation pressure, which depends on the emitted luminosity.
Conclusions. We derive mass outflow rates of about 6-700 $M_\odot$ yr^{-1} for our sample, which are lower than those observed in molecular outflows. Indeed physical properties of ionised outflows show dependences on AGN luminosity which are similar to those of molecular outflows but indicating that the mass of ionised gas is smaller than that of the molecular one. Alternatively, this discrepancy between ionised and molecular outflows could be explained with different acceleration mechanisms.

Key words. galaxies: active - galaxies: evolution - quasars: emission lines - techniques: imaging spectroscopy

1. Introduction

Feedback mechanisms from quasars (QSOs) are considered to be crucial for galaxy evolution (see King 2010, Fabian 2012 and King & Pounds 2015). During the bright active phase, Active Galactic Nuclei (AGN) are believed to drive energetic outflows that expel gas at large scales from their host galaxies (e.g Granato et al. 2004, Di Matteo et al. 2005, Menci et al. 2008, King 2010, Zubovas & King 2012, Fabian 2012, Faucher-Giguère & Quataert 2012, Zubovas & King 2014, Nayakshin 2014, Costa et al. 2014, Costa et al. 2015), hence removing the

supply of cold gas required for star formation (SF) activity. According to some of these models, the black hole (BH) achieves a critical mass during the later stages of a merging event and the energy output of the associated AGN is so large that radiation pressure drives a fast outflow in the nuclear region which sweeps away the gas in the host galaxy. When the feedback phase is over, the stellar population in the host galaxy continues to grow mainly through minor or major mergers with other galaxies. (e.g. Baldry et al. 2004, Pérez-González et al. 2008). At the same time the lack of gas around the nucleus slows down the growth of the BH. Models invoke feedback mechanisms to explain the origin of the correlation between the mass of supermassive BHs and the mass and velocity dispersion of host galaxy bulges observed in the local Universe (e.g. Magorrian et al. 1998; Marconi & Hunt

2003; Ferrarese & Ford 2005; Kormendy & Ho 2013). Essentially, the observed correlations can be explained as the result of the balance between the outward radiation force generated by the AGN and the inward gravitional force of the host galaxy (e.g. King 2010; Fabian 2012).

Quasar-driven outflows extending to kpc-scales have been resolved both locally (e.g Feruglio et al. 2010; Rupke & Veilleux 2011; Cicone et al. 2012; Rupke & Veilleux 2013; Rodríguez Zaurín et al. 2013; Feruglio et al. 2013b,a; Cicone et al. 2014; Rodríguez Zaurín et al. 2014; Aalto et al. 2015; Feruglio et al. 2015) and at high redshift (e.g. Alexander et al. 2010; Nesvadba et al. 2011; Harrison et al. 2012; Maiolino et al. 2012; Cano-Díaz et al. 2012; Harrison et al. 2014; Cresci et al. 2015; Cicone et al. 2015) in ionised, atomic and molecular gas. Despite big advances in data quality and analysis in the past decade, the main properties of these energetic outflows remain largely unknown. The exact outflow morphologies and driving mechanisms are still poorly known: it is debated whether their morphology is conical or shell-like, and it is also unclear what is the physical process responsible for the coupling of the energy/momentum released by the central AGN with the galaxy interstellar medium (e.g. inner winds and shocks, radiation pressure on dust). According to one of such scenarios, the fast wind, accelerated close to the BH by radiation pressure, shocks the ISM of the host galaxy creating a bubble of hot gas which expands at large velocities (~ 1000 km/s). If the post shock material does not cool efficiently, energy is conserved, the bubble expands adiabatically and the outflow is energy-driven. On the other hand, if the post shock material cools efficiently, due for example to Compton cooling by AGN photons, only momentum is conserved and the outflow is momentum-driven. Since the efficiency of the cooling process, dominated by inverse Compton scattering, drops with increasing shock radius, there is a critical distance (~ 100 pc - 1 kpc) beyond which the extended outflows can only be energy-driven (Zubovas & King 2012). Indeed, recent observations of kpc-scale outflows in local AGNs support this scenario (Cicone et al. 2014, Feruglio et al. 2015, Tombesi et al. 2015).

Moreover it is not clear whether molecular and ionised outflows are accelerated by the same mechanism, whether they have the same spatial distribution or whether they occur on similar timescales. So far, there are only a few observations of both molecular and ionised AGN-driven outflows in the same galaxy: SDSS J1356+1026 is an example of an obscured QSO where molecular and ionised outflows have different properties, i.e. outflow rates, velocities, radii, morphologies and time scales (Greene et al. 2012; Sun et al. 2014).

The forbidden emission line doublet [OIII] at $\lambda = 5007, 4959$Å is a good tracer of ionised outflows on large scales since it can not be produced at high densities and so it cannot trace the sub-parsec scales of the Broad Line Region (BLR). In the presence of outflows, the spectral profile of the [OIII]$\lambda5007$ emission line can be highly asymmetric, with a broad, blue-shifted wing that is rarely observed in star-forming regions. For this reason, the [OIII]$\lambda5007$ emission line has been used to identify outflowing ionised gas in low-redshift and high-z AGNs. Recent integral field observations of the [OIII]$\lambda5007$ emission have provided quantitative measurements of the outflowing gas properties in AGN at low redshifts $z < 0.5$ (e.g. Greene et al. 2011; Harrison et al. 2014). At higher redshift, $z \sim 2$, Alexander et al. (2010) found evidence for galactic-scale ionised outflows by mapping the [OIII]$\lambda5007$ emission line in ULIRGs (Ultra Luminous IR Galaxies) hosting type 1 AGNs. Cano-Díaz et al. (2012) observed a ionised outflow, extended up to ~8 kpc, in a QSO at $z \sim 2.4$. Finally, Brusa et al. (2015) and Perna et al. (2015)

detected broad [OIII]$\lambda5007$ blue wings in a sample of obscured AGN revealing the presence of outflows extended over several kiloparsecs. In one case of the latter sample, the ionised outflow, extended up to ~ 12 kpc, is anti-correlated with the presence of star formation in the host galaxy (Cresci et al. 2015), similarly to what found by Cano-Díaz et al. (2012).

In this paper, we present a kinematical analysis of the [OIII]$\lambda5007$ emission line observed in six high luminous ($L_{bol} > 10^{47}$ erg/s) quasars at $z \sim 2.4$. The line profiles and the velocity maps obtained by the kinematical analysis show the presence of ionised outflows extended on scales larger than $2-3$ kpc from the nucleus. This is one of the first observations of extended ionised outflows in QSO or type 1 AGN; indeed most AGN-driven outflows have been observed so far in type 2 AGN. We present a new method to measure outflow properties from IFU (Integral-Field Unit) data when the source is only marginally spatially resolved. We show that the typical signature of outflows, i.e. asymmetric line profiles and blue-shifted components in the velocity maps, can be described by two point sources (the central AGN source and the outflowing material) separated by a distance of a few kpc. We find that the ionised gas likely traces only a fraction of the total outflowing gas, unless ionised outflows have a different origin than the molecular ones.

The paper is organised as follows: in Section 2 we present the sample selection and properties, in Section 3 we show the data analysis and spectral fitting. The results of our data analysis are presented in Section 4. Finally, in Section 5 we discuss the main results, i.e. the nature of ionised outflows and the comparison with other observations. A $H_0 = 67.3$ km s^{-1} Mpc^{-1}, $\Omega_M = 0.315$, $\Omega_\Lambda = 0.685$ cosmology is adopted throughout this work (Planck Collaboration et al. 2014).

2. Sample selection

We selected six QSOs at $z \sim 2.4$ with large [OIII]$\lambda5007$ equivalent widths (> 10Å in the rest frame) and bright H-band magnitude (< 16.5 mag) from the sample of Shemmer et al. (2004), Netzer et al. (2004) and Marziani et al. (2009). The luminosities of the objects in our sample are in the range $L = 10^{47} - 10^{48}$ erg/s, making them the highest luminosity sources where outflows have been spatially mapped. These characteristics are chosen to maximise our chances to detect signatures of feedback on the host galaxy. As explained in Section 1, the cosmic epoch corresponding to $z \simeq 2$ is crucial for the growth of the most massive galaxies and black holes, and shows the maximum activity both in star formation and in BH accretion (e.g., Madau & Dickinson 2014). The selected objects, at the high end of the QSO luminosity function, are those where we expect to detect feedback in action, at least according to current galaxy evolutionary models (e.g. Hopkins et al. 2006). Moreover, the targets were selected depending on their particular [OIII] profile. Indeed, the large [OIII]$\lambda5007$ equivalent width should allow us to easily recover the kinematical maps of the ionised gas, a challenging task in luminous QSOs where narrow emission lines are usually weak (e.g Netzer et al. 2004). Finally, the bright ionised line profile can be easily deblended from the broad Hβ and FeII emission, which are associated to the BLR. Indeed, based on near-IR spectra available from the literature (Shemmer et al. 2004; Netzer et al. 2004; Marziani et al. 2009), we also chose our objects such that the contamination from broad FeII emission is expected to be small.

Basic properties of the observed objects are given in Table 1. One of our sources, 2QZJ0028, is already studied by Cano-Díaz et al. (2012), and was reobserved by using much longer integration time, confirming their results.

3. Observations and data reduction

The targets, whose properties are described in Table 1, were observed in February and September 2012 using the near-IR integral field spectrometer SINFONI (Spectrograph for INtegral Field Observations in the Near Infrared) at the VLT (Very Large Telescope). The observations were obtained in H-band ($\lambda \sim 1.45 - 1.85\,\mu m$, where [OIII]$\lambda 5007$, [OIII]4959 and H$\beta$ are detected), in seeing limited mode with 0.250″ spatial scale and medium spectral resolution of R = 3000. In all observations, the object was moved across the 8″×8″ field of view in order to perform the sky subtraction. A standard star for telluric correction and flux calibration was observed shortly after or before the on-source exposures. The total on-source integration time is over 3h per target. The airmass are different for each target and spanning a range between ~ 1.0 and ~ 1.4.

After removing cosmic rays from the raw data using the L.A. Cosmic procedure (van Dokkum 2001), we used the ESO-SINFONI pipeline to reduce the data. The final data cubes produced by the ESO-SINFONI pipeline have a spatial scale of 0.125″×0.125″ and a field of view of about 8″×8″. The estimated angular resolution is $\sim 0.4 - 0.6$″, based on a 2D-Gauusian fitting of the flux map of the spatially unresolved broad Hβ line (see Section 4.1).

4. Data analysis

Figure 1 shows the H-band spectra extracted from the nuclear region of each QSO from an aperture of 0.25″×0.25″. The spectra clearly show the broad Hβ and the strong emission line doublet [OIII]$\lambda\lambda 5007, 4959$. In addition to these components, weak FeII emission lines are also visible in two out of the six QSOs (LBQS0109 and HE0251). The asymmetric [OIII]$\lambda 5007$ profiles suggest the presence of ionised outflows in most of the targets (LBQS0109, 2QZJ0028, HB8905, HB8903 and HE0251). Indeed the presence of a prominent blue wing is the typical signature of high velocity gas moving toward the line of sight. The Hβ emission line shows asymmetric velocity profiles as well as, in some cases, two distinct emission peaks (i.e HB8903). Indeed, in all spectra the Hβ line is a sum of two different components: a very broad ($FWHM > 2000$ km/s) one which is associated to the BLR emission and a fainter, narrower ($FWHM\sim$ 500-1200 km/s) one likely associated to NLR emission.

4.1. Fitting procedure

In order to understand the dynamic and the main properties of the ionised outflows, we performed a kinematical analysis on the forbidden lines.

At first, we extracted the spectrum of each QSO from a nuclear region of 0.25″×0.25″ where the signal-to-noise (S/N) is highest. We fitted simultaneously the continuum, Hβ and [OIII] emission lines by minimizing χ^2 using the IDL routine MPFIT (Markwardt 2009).

The [OIII]$\lambda 5007$ line profile is very complex in these objects and a single Gaussian function is not able to reproduce the asymmetric velocity profiles, so we fitted the emission-line doublet using either multiple Gaussian components or a broken power-law convolved with a Gaussian distribution. Initially, we fitted the emission line using two Gaussian components, one broad (FWHM > 1000 km/s) and one narrow (FWHM < 1000 km/s), and, when necessary, added a third component to minimise the χ^2 value. Since in a few cases the [OIII]$\lambda 5007$ emission line exhibits a very asymmetric line profile with blue wings extended

to $|v| >$1000 km/s, we replaced the multi-Gaussian components with a broken power-law profile convolved with a Gaussian distribution. We did not add additional Gaussian components in order to avoid an unnecessary large number of free fitting parameters. We do not attribute any physical meaning to the individual fitting component and we measure gas kinematics by analysing the total line profile. Therefore, using either multiple Gaussian components or a broken-power law does not change the results of this work, provided that the quality of the fit is similar. The two emission lines of the [OIII] doublet, originating from the same upper level, were fitted imposing the same central velocity and velocity dispersion, with the intensity ratio $I(5007)/I(4959)$ fixed at ~ 3.

Hβ is well described by two components, a broad (BLR) and a narrow one (NLR). We used a broken power-law profile for the very broad component (FWHM > 2000 km/s) since it usually provides a good fit to QSO broad emission lines (Nagao et al. 2006). The model used for the Hβ profile of 2QZJ0028 shows a broad red wing that is likely due to continuum or FeII emission, so we do not attribute any physical meaning to this red-shifted emission. A similar profile is visible in Figure 1 of Cano-Díaz et al. (2012). Since the narrower Hβ is weak and sometimes only marginally detected, it is not possible to reliably constrain its profile and kinematics and therefore we assume that it has the same average velocity and velocity profile as [OIII]$\lambda 5007$.

Finally we used a power-law for the continuum and, for those spectra showing FeII emission, we used the FeII template from Tsuzuki et al. (2006). These best-fitting solutions are used as first guesses in the pixel-to-pixel fitting of the kinematical analysis described in the following.

Before performing a spatially resolved kinematical analysis, we tested whether the kinematics of the ionised gas is spatially resolved. Following the method described in Carniani et al. (2013), we analysed the flux residual maps obtained with a pixel-by-pixel kinematical fitting with the components just described, after assuming that the targets are spatially unresolved. In this case, the H-band spectrum is expected to be the same in any spaxel apart for a different normalisation. The residual maps (Figure 2) at the wavelength range of [OIII]$\lambda 5007$ indicates that the forbidden line emission is kinematically resolved in all but one of the quasars, i.e HE0251. In fact, if the emission was unresolved, we would expect to observe both a spectral profile and a residual map consistent with the noise, as in the case of HE0251. The flat residual at the wavelength range of Hβ indicates that the broad component of Hβ is spatially unresolved, consistently with a Hβ origin in the BLR.

After testing that the [OIII]$\lambda 5007$ line emission is kinematically resolved in five of the six sampled QSOs, we performed a pixel-by-pixel fitting on the data cubes allowing the spectral components to vary except for the broad Hβ which is not spatially resolved. Figure 3 shows the kinematical properties of the ionised gas as obtained from the fit of the [OIII]$\lambda 5007$ line:

- zeroth moment map (i.e., line flux map; first panel);
- first moment map (i.e., median velocity map; second panel);
- blueshifted velocity map, v_{10}, the velocity at the 10th percentile of the overall emission-line profile (third panel); fitted in each spatial pixel;
- line width map , W_{80}, the velocity width of the line that contains 80% of the emission-line flux (fourth panel); this is defined as $W_{80} = v_{90} - v_{10}$, where v_{10} and v_{90} are the velocities at 10th and 90th percentiles, respectively. For a Gaussian profile, W_{80} is approximately the full width at half maximum (FWHM).

Table 1. Properties of our quasar sample

ID	Target Name	λ_0 [μm]	$\Delta\lambda_{rest}$ [Å]	Redshift	λL_{5100} [10^{46} erg/s]
LBQS0109	LBQS 0109+0213	1.68 ± 0.04	28.5 ± 0.2	2.35 ± 0.08	4.9 ± 0.8
2QZJ0028	2QZ J0028-2830[(a)]	1.70 ± 0.04	27.9 ± 0.2	2.40 ± 0.09	3.1 ± 0.6
HB8905	HB89 0504+030	1.75 ± 0.05	22.7 ± 0.2	2.48 ± 0.09	2.9 ± 0.6
HE0109	HE 0109-3518	1.706 ± 0.003	17.342 ± 0.011	2.407 ± 0.007	7.4 ± 1.5
HB8903	HB89 0329-385	1.720 ± 0.013	19.31 ± 0.06	2.44 ± 0.03	5 ± 2
HE0251	HE 0251-5550	1.68 ± 0.03	31.81 ± 0.17	2.35 ± 0.05	6.8 ± 1.4

(a): this is the same target of Cano-Díaz et al. (2012) which has been re-observed.
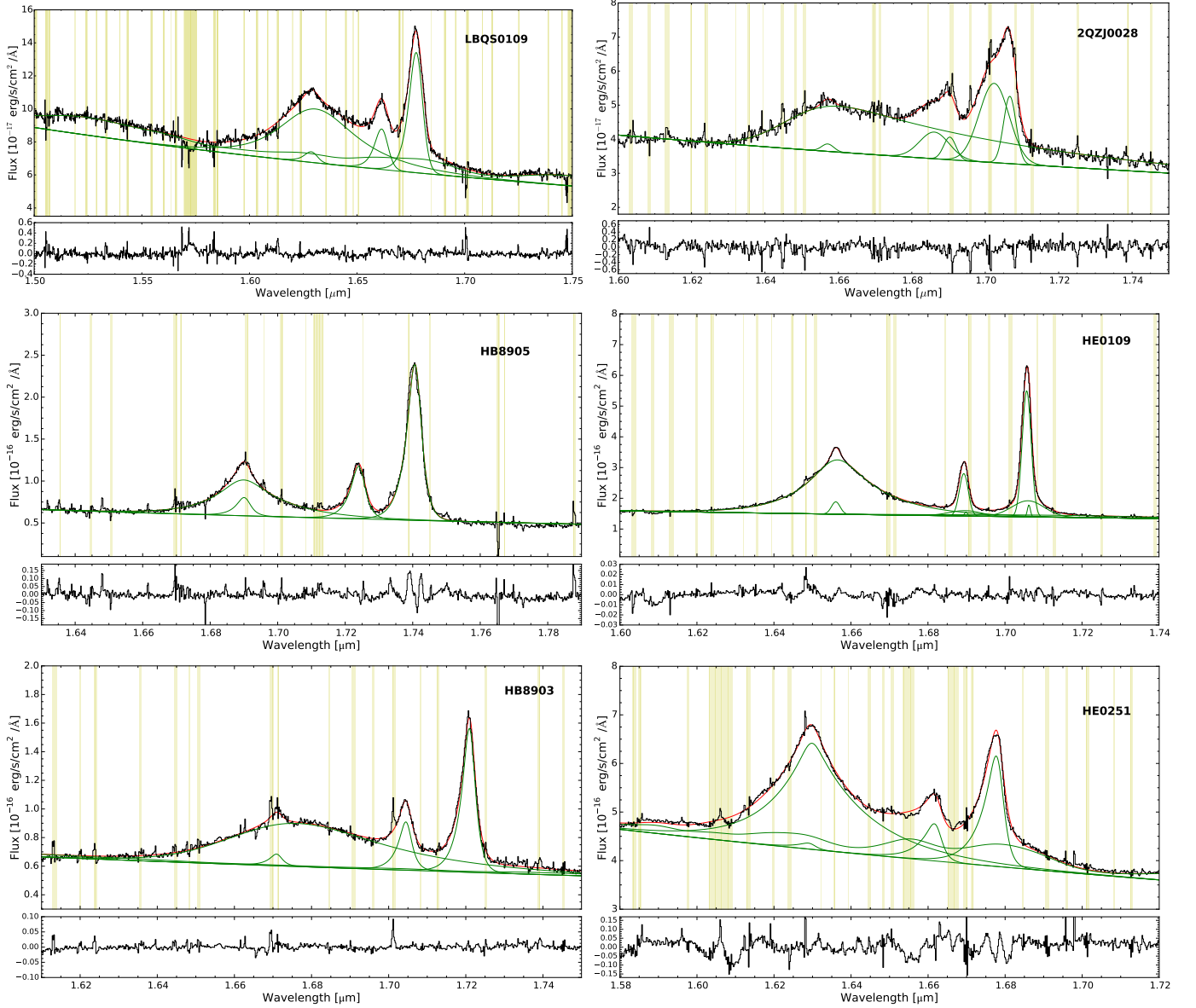
Fig. 1. *Upper panel*: The spectra of the six QSOs if our sample. Each spectrum is extracted from a nuclear region of $0.25''\times025''$ (2×2 pixel). The different components in the fit for each line (Hβ,[Oɪɪɪ] and FeII) are shown in green and the red line is the total fit. The shaded yellow regions indicate the zone affected by strong sky line residuals which are excluded from the fit. *Lower panel*: fit residuals, obtained as a difference between observed and model spectra.

The observed kinematical maps are the results of the convolution of the intrinsic ones with the PSF of the observations. In those cases where the [Oɪɪɪ]λ5007 emission line has been fitted with multiple Gaussians, line profiles are based on the sum of all Gaussian components. The maps were obtained by selecting only those spatial pixels with a S/N equal to or higher than 2. We defined the S/N as the ratio between the peak of the [Oɪɪɪ]λ5007 line and the rms of the residuals. Zero-velocities correspond to the peak position either of the narrow (FWHM < 1000 km/s) and strongest Gaussian component or of the broken-power law one
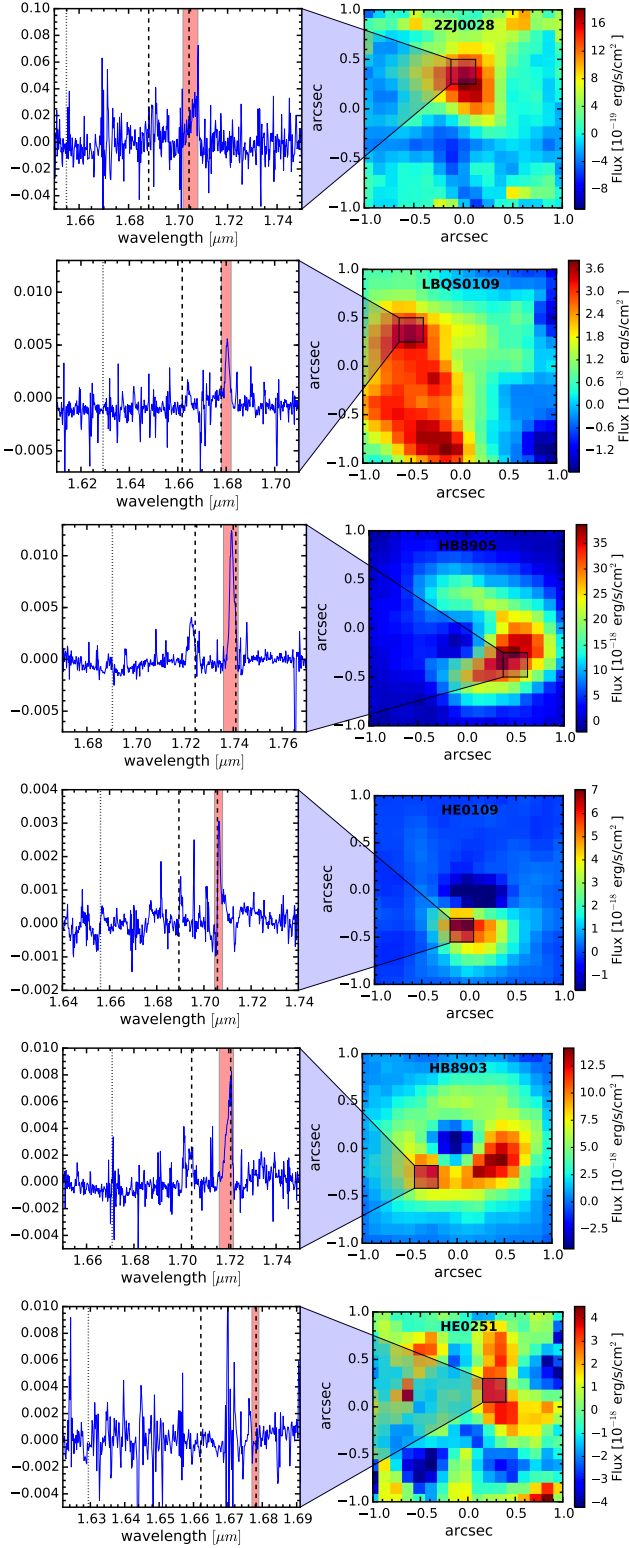
Fig. 2. Residuals from the pixel-per-pixel fitting assuming that the QSO emission is not spatially resolved. Left panels: residual spectra extracted from a region of $0.25'' \times 0.25''$, where the residual map, obtained by collapsing the [OIII]λ5007 spectral channel, shows likely the presence of a spatially resolved emission. Dashed lines indicate the wavelength of the doublet [OIII]λ5007 and the dotted line shows the Hβ position. The red shaded region denotes the wavelength range over which the residual [OIII]λ5007 emission has been integrated to produce the maps shown on the right. Right panels: residual maps obtained by collapsing the spectral channels corresponding to the residual [OIII]λ5007 emission, as shown by the red region in the left panels. In the first five maps the presence of a clear [OIII]λ5007 residual emission suggests that the emitting region is spatially resolved. The "noise" residual map of HE0251 indicates that the sources is not resolved.

of the [OIII]λ5007 profile estimated in the preliminary spectral fitting. The zero-velocity wavelength was also used to refine the redshift of each QSO (Table 1) providing the velocity of the host galaxy. The inferred redshift and [OIII]λ5007 line width are consistent, within the errors, with those estimated by Shemmer et al. (2004) and Marziani et al. (2009).

The v_{10} maps (Figure 3, third panel) show strongly blue shifted regions, spatially associated with high velocity dispersion (> 400 km/s, Figure 3, forth panels). The broad [OIII]λ5007 profile cannot be explained by a rotating gas component, which, in local star forming galaxies has typical FHWM values of about ~ 250 km/s. Moreover, the morpholgy of the velocity maps , suggesting the presence of a conical blue-shifted region, is completely different from the typical "spider" diagram of a disc. Consequently both the [OIII]λ5007 profile and the velocity maps suggest that in at least five out of six QSOs we detect ionised outflowing gas with velocities > 300 km/s.

We can detect only the blue-side outflows because the red-side is likely to be obscured by dust in the host galaxy along the line-of-sight. For this reason, the [OIII]λ5007 line emission is asymmetric with a prominent blue shifted wing. While this is what commonly happens, in some cases the particular orientation of the line-of-sight with respect to the source can result in redshifted outflows (e.g. Rodríguez Zaurín et al. 2013; Bae & Woo 2014; Perna et al. 2015).

The next step is to understand the physical mechanisms driving away the ionised gas out to a distance of a few kpc from the centre of the host galaxy.

5. Outflow properties

In the following, we estimate mass, average velocity and radius of the high-velocity winds. We then infer mass outflow rate, momentum rate and kinetic power, and compare them with previous works (Greene et al. 2012, Cicone et al. 2014, Harrison et al. 2014, Sun et al. 2014, Brusa et al. 2015, Cresci et al. 2015 and Feruglio et al. 2015).

5.1. Outflow and radius

Given the uncertainties on the driving mechanism, we used a simple model to estimate the physical properties of the outflow. In this model, the outflow is represented by a shell-like cloud ejected from the nucleus within a cone and with a filling factor equal to 100%. We assume that the physical size of the outflowing material is smaller than the spatial resolution typical of our datasets. This model is defined by the mass of the cloud, M_o, the distance between the cloud and the location of the AGN, R_o, and the averaged cloud velocity, v_o. The outflow mass rate is given by

$$\dot{M}_o = \frac{M_o}{\tau_{dyn}} = \frac{M_o v_o}{R_o} \tag{1}$$

where τ_{dyn} is the dynamical time, i.e. the time taken by the ionised gas to reach a distance R_o with an average velocity v_o. We note that assuming either a shell or a uniformly filled cone with a filling factor equal to 1 (e.g Maiolino et al. 2012) changes the $\dot{M}_o$ estimate by a factor of 3. Since this factor is constant, it does not affect the main conclusions of this work but we will take it into account when comparing our results with previous ones.

The extension of an outflow (R_o) is usually trivially estimated from the observed flux or velocity maps (e.g. Harrison et al.
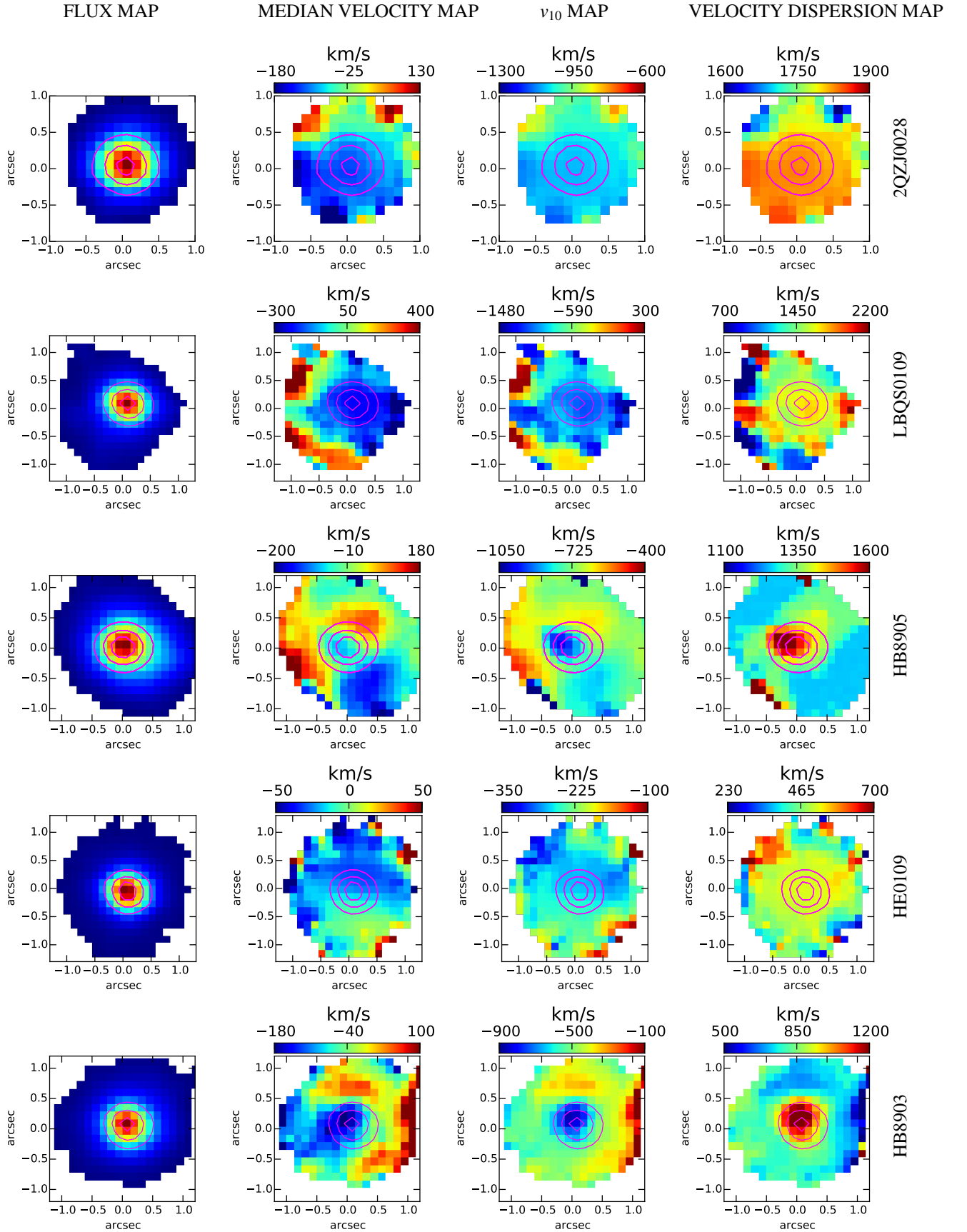
Fig. 3. [Oɪɪɪ]λ5007 flux, median velocity, v_{10}, and velocity dispersion map. The maps are obtained by selecting pixels with a SNR>2. The velocity maps are characterised by blue shifted regions with a large velocity dispersion. Contours represent the total Hβ line surface brightness at 90%, 50%, and 30% of the peak value

2014, Cresci et al. 2015). However, in our cases, the [OIII]λ5007 emission is only marginally spatially resolved in each QSO, therefore the kinematical maps in Figure 3 are affected by PSF smearing and the sizes of the regions showing blue-shifted emission (Fig. 3) do not directly provide the parameter R_o to be used in equation 1. Furthermore, the sizes of the outflowing regions are affected by the choice of S/N threshold adopted in plotting the maps. In particular, assuming a S/N threshold larger than 2, the blue regions would be smaller than those shown in Figure 3. For these reasons, we cannot estimate R_o from our observations by using the flux or velocity maps as in previous works, where emission lines are clearly spatially resolved. Therefore, we decided to estimate R_o by using spectroastrometry, which allows position measurements on scales smaller than the spatial resolution of the observations. Spectroastrometry consists in measuring the photo-centroid in each velocity channel. If outflowing ionised gas is moving away at a distance R from the QSO, we expect that the centroid of light emission extracted from blue-shifted velocities channels of [OIII]λ5007 will be displaced of the same amount R with respect to the QSO position, identified by the BLR and/or continuum emission. In Section 5.3, by means of a simple simulation, we show that spectroastrometry can, indeed, provide information on the outflow position at scales that are significantly smaller than the limit imposed by the spatial resolution of the observations.

We applied the spectroastrometry technique to the [OIII]λ5007 line emission after subtracting the best-fit model of the continuum, broad Hβ and FeII emission. To maximise the signal-to-noise ratio for our measurements and minimize the uncertainty due the spectral resolution, we rebinned the spectra by 3 velocity channels ($\sim$ 105 km/s). The centroid of the [OIII]λ5007 emission in each rebinned velocity channels was, then, estimated by a 2-dimensional Gaussian fitting. The QSO position was estimated by applying the same spectroastrometry technique to the the continuum and the broad Hβ emission.

The results of the spectroastrometric analysis are displayed in Figure 4. In the left panels, we plot the distance R of the emission line photocenter from the continuum one as a function of velocity v. The right panels show the photocenter position on the sky in each velocity channel. The reliable spectroastrometric measurements for the [OIII]λ5007 emission line were selected to satisfy the following criteria:

○ signal-to-noise larger than 1.5 for the line flux in each spectral channel of the rebinned spectra extracted from a 0.25″ × 0.25″

○ FWHM of the 2-dimensional Gaussian equal or larger than that of the PSF of the observations

In all targets, the [OIII]λ5007 blue wings centroids are displaced at least 0.05″, i.e. 0.4 kpc, from the continuum position and, in some cases, we observe an offset in the red wavelengths as well. This latter offset may be caused by three reasons: (i) the continuum is not well subtracted during the kinematic analysis; (ii) the [OIII]λ5007 emission line associated to outflows is so large that the displacement is slightly observable also in the red wings; (iii) the red wings are emitted by the receding outflows not completely obscured by dust in the disc. An additional explanation, which will be discussed in a companion paper is that in two out of six QSOs a fraction of the red [OIII]λ5007 line emission is associated with star formation in the host galaxy causing a displacement from the continuum centre.

Since the position of the photocenter at high blue velocities reveals the presence of the extended ionised outflow, we adopt R_o equal to the largest distance measured for the approaching
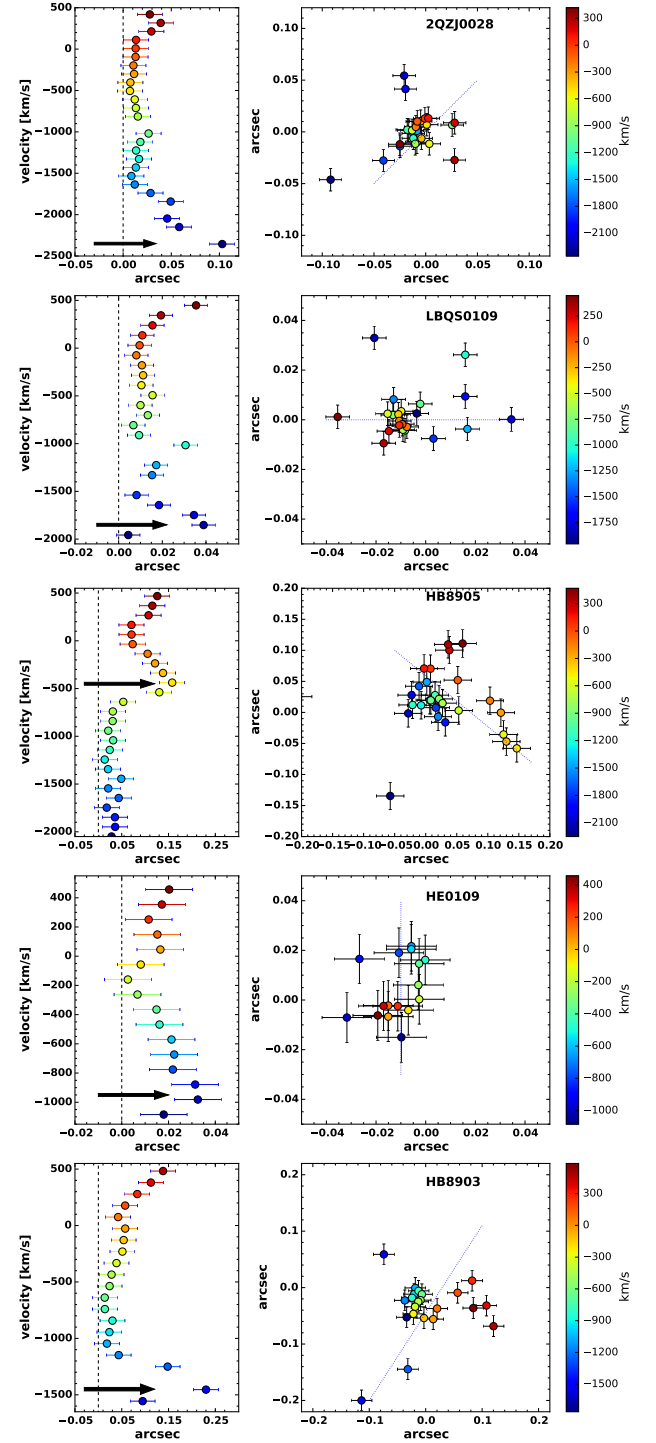

Fig. 4. Left panels. The points show the [OIII]λ5007 velocity v versus the distance R of the [OIII]λ5007 photocenter from the continuum (indicated by the dashed line). The arrows indicate the velocity $v_o = v(R_o)$ corresponding to the distance R_0. Right panels. The [OIII]λ5007 photocenter position in the field of view. Symbols are coloured according to their velocity (the velocity scale is reported in the colour bar). The dotted line indicates the project direction of the outflow as inferred by comparing the spectroastrometry results with velocity maps (Fig. 3).

gas, and $v_o = v(R_0)$ as measured from our maps (see arrows in Figure 4). Since the spectra have been rebinned by 3 velocity channels, the error on v_0 due to the spectral resolution typical of our datasets is negligible. R_o and v_o for each quasar are listed in Table 2.

Table 2. Outflow properties

QSO	v_o [km/s]	R_o [kpc]	$\text{Log}(L_{[OIII]}^{outflow})$	$\text{Log}(L_{H\beta}^{outflow})$	$M_{[OIII]}^{outflow}$ [10^7 M$_\odot$]	$M_{H\beta}^{outflow}$ [10^7 M$_\odot$]	$\dot{M}_{[OIII]}$ [M$_\odot$ yr^{-1}]	$\dot{M}_{H\beta}$ [M$_\odot$ yr^{-1}]
LBQS0109	1850	0.4	43.17	42.10	1.2	2.2	60	110
2QZJ0028	2300	0.7	43.68	43.07	3.8	20	140	700
HB8905	500	1.3	43.95	42.99	7.1	16.8	30	75
HE0109	900	0.4	43.75	42.71	4.5	8.6	110	210
HB8903	1450	1.9	42.95	41.8	0.7	1.2	6	10
HE0251	-	-	43.82	42.55	5.3	6.1	-	-

Notes: The outflow masses are estimated assuming a $T_e \sim 10^4$ K and a $n_e \sim 500$cm^{-3}.

5.2. Outflow Mass

A big challenge in estimating the mass of the wind is caused by its multiphase nature. Indeed, only a fraction of the mass of the outflows is in the warm ionised phase traced by [OIII]λ5007. Recent works estimate the mass of ionised outflows either using Hβ emission line (e.g Liu et al. 2013; Harrison et al. 2014) or using [OIII]λ5007 line (e.g Cano-Díaz et al. 2012). So far, it is not clear which is the best tracer of ionised gas powered by AGN feedback. To compare two different measurements carried out with these two different tracers, we discuss how the mass of ionised outflows can be constrained through the observations of [OIII]λ5007 and Hβ.

The [OIII]λ5007 luminosity is given by

$$L_{[OIII]} = \int_V f n_e n(O^{2+}) j_{[OIII]}(n_e, T_e) dV \tag{2}$$

where f is the filling factor, n_e the electron density, $n(O^{2+})$ the density of O^{2+} ions and $j_{[OIII]}(n_e, T_e)$ the line emissivity. $n(O^{2+})$ can be written as

$$n(O^{2+}) = \left[\frac{n(O^{2+})}{n(O)}\right]\left[\frac{n(O)}{n(H)}\right]\left[\frac{n(H)}{n_e}\right] n_e$$

and, with a reasonable assumptions, $n(O^{2+}) = n(O)$,

$$n(O^{2+}) \simeq (6.04 \times 10^{-4} 10^{[O/H]-[O/H]_\odot}) \times (1.2)^{-1} \times n_e$$

where $[O/H] - [O/H]_\odot$ is the metallicity relative to solar with a solar oxygen abundance of $[O/H]_\odot \sim 8.86$ (Centeno & Socas-Navarro 2008). The factor $(1.2)^{-1}$ takes into account a 10% number density of He atoms with respect to H atoms:

$$n_e \approx n(H) + 2n(He) = n(H) + 2 \times 0.1 \times n(H) = 1.2n(H)$$

Assuming a typical temperature ($T_e \simeq 10^4 K$) and electron density ($n_e \simeq 500$ cm^{-3}) for the NLR the line emissivity is

$$j_{[OIII]} = 3.4 \times 10^{-21} \text{ erg s}^{-1}\text{cm}^{-3}$$

This line emissivity was estimated making use of PyNeb (Luridiana et al. 2015). Therefore, equation (2) can be rewritten as:

$$L_{[OIII]} = 6.0 \times 10^{-4} f 10^{[O/H]-[O/H]_\odot} j_{[OIII]} < n_e^2 > V \tag{3}$$

where $< n_e^2 >$ is the volume-averaged squared density. The gas mass can be expressed as

$$M \simeq \int_V f\overline{m}n(H)dV \simeq f m_p < n_e > V \tag{4}$$

where $\overline{m}$ is the average molecular weight, m_p is the proton mass, and we have taken into count that a 10% number density of He atoms with respect to H atoms:

$$\overline{m}n(H) \approx \frac{m_p n(H) + 4m_p n(He)}{n(H) + n(He)} \frac{n(H)}{n_e} n_e$$

$$\approx \frac{n(H) + 0.4n(H)}{n(H) + 0.1n(H)} m_p (1.2)^{-1} n_e \approx 1.2 m_p (1.2)^{-1} n_e = m_p n_e$$

Finally, combining equation (3) and equation (4) we get:

$$M_{[OIII]} = 1.7 \times 10^3 \frac{m_p C L_{[OIII]}}{10^{[O/H]-[O/H]_\odot} j_{[OIII]} < n_e >} \tag{5}$$

where $C = < n_e >^2 / < n_e^2 >$. For $T_e = 10^4$ K and $n_e = 500$ cm^{-3} we obtain a mass of:

$$M_{[OIII]} = 0.8 \times 10^8 \text{M}_\odot \left(\frac{C}{10^{[O/H]-[O/H]_\odot}}\right)\left(\frac{L_{[OIII]}}{10^{44}erg/s}\right)\left(\frac{< n_e >}{500cm^{-3}}\right)^{-1}$$

Note that the gas mass is sensitive to temperature and density of the clouds.

Now we similarly derive M from Hβ. The Hβ luminosity can be expressed as

$$L_{H\beta} = \int_V f n_e n_p j_{H\beta}(n_e, T_e) dV \simeq 1.2^{-1} f j_{H\beta}(n_e, T_e) < n_e^2 > V \tag{6}$$

where $j_{H\beta}$ is line emissivity and n_p is the proton density that can be written as

$$n_p = \left[\frac{n(H)}{n_e}\right] n_e = (1.2)^{-1} n_e$$

At the typical temperature and density of the NLR, the line emissivity of Hβ also estimated with PyNeb is

$$j_{H\beta} = 1.2 \times 10^{-25} \text{ erg s}^{-1}\text{cm}^{-3}$$

Combining equation (4) with equation (6) of $L_{H\beta}$ we get

$$M_{H\beta} \simeq 0.8 \frac{m_p C L_{H\beta}}{j_{H\beta} < n_e >} \tag{7}$$

For $T_e \sim 10^4$ K and $n_e \sim 500$ cm^{-3} we obtain a mass of:

$$M_{H\beta} = 1.7 \times 10^9 \text{M}_\odot \, C \left(\frac{L_{H\beta}}{10^{44}erg/s}\right)\left(\frac{< n_e >}{500cm^{-3}}\right)^{-1}$$
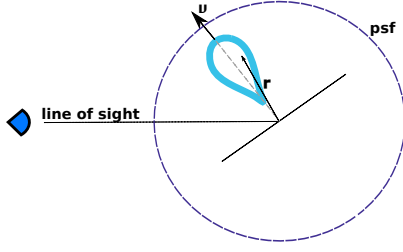
Fig. 5. Cartoon showing the basic structure of our model. The outflow (solid blue curve) is perpendicular to the galaxy plane. v indicates the direction of the outflow and r is the distance from the QSO. This model assumes that the outflow is marginally resolved but it is not larger than the PSF dimension (dashed purple line).

Comparing the two mass at the same temperature and density, we get

$$\frac{M_{[OIII]}}{M_{H\beta}} \simeq 0.05 \frac{L_{[OIII]}}{L_{H\beta}} \qquad (8)$$

with [O/H] = [O/H]$_\odot$, T$_e \sim 10^4$ K and n$_e \sim 500$ cm^{-3}, the same values which will be assumed in the following analysis. Usually the [OIII]λ5007/Hβ ratio measured in Seyfert galaxies is of the order of ~ 10 providing $M_{[OIII]}/M_{H\beta} \sim 0.5$. This apparent discrepancy is the consequence of the different volumes from which [OIII]λ5007 and Hβ are emitted: in the above example the volume of Hβ emitting gas is ~ 2 larger than that of [OIII]λ5007. Therefore, Hβ emission traces a larger amount of ionised gas mass than [OIII]λ5007. The mass estimated from [OIII]λ5007 will then be considered as a lower limit on the ionised gas mass.

5.3. Simulations of spectroastrometric observations of outflows

In Section 5.1 we have described our method to estimate R_o, which is not affected by the spatial resolution of the data and on the S/N threshold used to map velocities.

In the following we present results of simple simulations of outflowing gas, validating the spectroastrometric method. Note that the purpose of this work is not to build an outflow model to fit our observations, but the only purpose of this simulation is to show that the extension of the flux or velocity maps when the source is marginally resolved can provide wrong estimates of the outflow extension due to PSF smearing. In fact we will also show that an ionised clump with a given velocity and located a few kpc away from the AGN can appear as a blue-shifted region extended over ~ 5-10 kpc in velocity maps, which is larger than the real outflow extension.

We considered a simple model of an outflow (Fig. 5) based on the following assumptions.

1. The outflow has a biconical geometry with the axis approximately more or less perpendicular to the host galaxy disk; indeed, the AGN wind, although roughly isotropic, cannot propagate through the galaxy disk because of its high density.
2. The receding half cone is not observed because its emission is absorbed by the dust in the host galaxy. This geometry best explains the asymmetric [OIII]λ5007 profile with a prominent blue wing over 1000 km/s.
3. The surface brightness distribution of the outflow is parameterised by

$$I(r) = I_0 e^{-r/R_o^{model}}$$

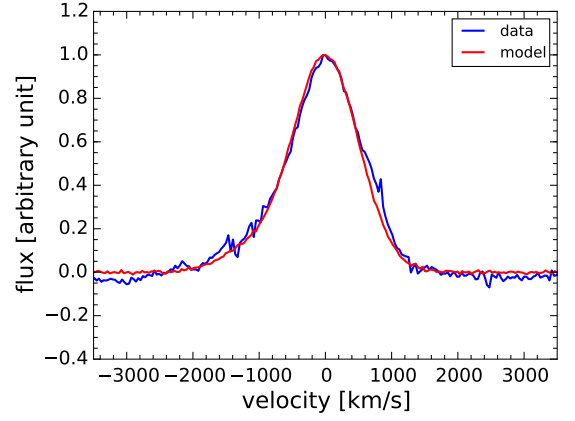**Fig. 6.** [OIII]λ5007 emission lines extracted from a nuclear region of 0.25″× 0.25″ . The blue line is the [OIII]λ5007 emission line of LBQS0109 after subtracting all the other best-fit components. The red line is the ionised emission line obtained from the simulated data.

where the vector r is the distance from the QSO. Note that the surface brightness distribution and the opening angle of the cone are not fundamental for these simulations, since the spatial resolution of our data is not high enough to resolve the surface brightness profile. We assume an opening angle of 30 degrees. R_o^{model} identifies the photo-center of the surface brightness of the ionised cloud. I_0 is proportional to the outflow mass M_o^{model} defined in equation (4).

4. The ionised gas in the outflow has an average velocity v_o^{model} and a velocity dispersion σ_o^{model}.

Therefore the input parameters are the outflow mass M_o^{model}, the distance R_o^{model} of the ionised clouds from the centre of the QSO, the average velocity v_o^{model} and the velocity dispersion σ_o^{model} of the ionised gas.

In order to reproduce the [OIII]λ5007 line profile of LBQS0109 we simulated a QSO with an outflow characterised by $M_o^{model} = 1.0 \times 10^7$ M$_\odot$ (eq. 5), $R_o^{model} = 0.05$ arcsec (i.e $\sim$0.4 kpc), $v_o^{model} = 1500$ km/s and $\sigma_o^{model} = 500$ km/s. We also considered a point source at the location of the AGN describing the gas at the systemic velocity with velocity dispersion ~ 400 km/s and an amplitude scaled as to reproduce the observed line profile. The total [OIII]λ5007 emission was then projected onto the sky plane, assuming a galaxy disc inclination of 10 degrees, i.e. almost face on as typical of QSO. Finally we convolved the surface brightness maps in each spectral channel with the PSF and added Gaussian noise to match the sensitivity of our observations.

The comparison between the [OIII]λ5007 line profile extracted from the simulated data and that from the observations is shown in Figure 6. Both spectra are extracted from a nuclear region of 0.25″× 0.25″. The simulated emission line presents a prominent blue wings similarly to the real spectrum of LBQS0109. We then performed the kinematic analysis on the simulated data as described in Section 4.1. The flux, velocity and velocity dispersion maps (Fig. 7) obtained from the simulations are similar to those shown in Figure 3 extracted from observations. Indeed, the velocity map shows blue shifted velocities in the outflow region extended over 0.5 ″(i.e ~4.2 kpc). So, the simulation confirms that the blue-shifted region suffers from beam smearing and its size does not match the real radius of the outflow.

Since the simulated outflow well describes the asymmetric [OIII]λ5007 profile and the velocity gradient observed in our datasets, we carried out the spectroastrometry analysis on the
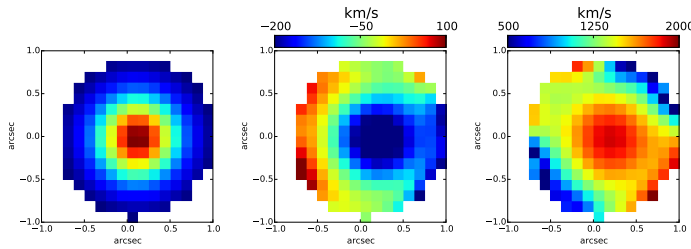
Fig. 7. [OIII] flux, velocity and velocity dispersion map obtained from the simulated [OIII]λ5007 data. The regions with S/N < 2 are masked out.

Fig. 8. Spectroastrometry results obtained from the simulated data. On the left, centroid offset of [OIII]λ5007 emission respect to continuum emission (dashed line) at different wavelength. On the right, the photo-centroid position in each velocity. Colour coding corresponds to velocity offset.

simulated data to estimate the average velocity and radius of the ionised gas in order to compare these derived values with the input parameters. The offset of the photo-centroids at different velocities are shown in Figure 8. The radius R_o (~ 0.05 ″) and the average velocity $v(R_o)$ (~ 1450 km/s) estimated from spectroastrometry are consistent to the initial input parameters. So, provided that the S/N is high enough, the spectroastrometry method can provide the position and the velocity of outflows with an accuracy well below the seeing limit. Moreover, since the integral flux of [OIII]λ5007 at high blue-shifted velocity (-2500km/s $< v < v(R_o)$) is consistent with about half of the total flux emitted from the ionised outflowing gas, the outflow luminosity can be inferred from:

$$L_o = 2 \int_{-\infty}^{\lambda_0} L_\lambda(\lambda)d\lambda \qquad (9)$$

where λ_0 is the wavelength corresponding to v_0. In the cases where the [OIII]λ5007 emission line was well described by a multi-Gaussian fit, the luminosity value calculated with equation (9) and the one estimated from the broad Gaussian component, as typically done in the literature, are consistent within the errors. So, in the multi-Gaussian fit we estimated the L_o from the broad component and in the other case we measured the luminosity of the gas using the equation (9).

Since the narrow Hβ component has the same profile of [OIII], we can measure the outflow luminosity for both the emission lines using the same equation. From the luminosity we can get the mass of the ionised outflows by using equation (4) and (7). As the [OIII]λ5007/Hβ ratio measured in each QSO is $\sim$ 10, the mass inferred by Hβ is $\sim$ 2 times larger than that estimated by [OIII]λ5007 (see eq. 8). The luminosity and mass of the outflow are listed in Table 1 and 2, respectively. Since HE0251 is not spatially resolved, we cannot estimate the outflow luminosity using the method described above. In this case we fitted the [OIII]λ5007 with two Gaussian components and we inferred the outflow luminosity from the broad Gaussian component.

6. Results

In order to investigate the nature of the ionised wind, we need to estimate the main quantities of the outflows: mass outflow rate, momentum rate and kinetic power. Theoretical models (e.g Zubovas & King 2012, Faucher-Giguère & Quataert 2012) predict tight relations between these quantities and the AGN bolometric luminosity, L_{AGN}. In particular the correlation between the momentum rate and L_{AGN} provides an indicator of the nature of the feedback mechanism. In this section we derive the main properties of the AGNs in our sample and compare them with the prediction of the models. As explained in Section 5.3, the low spatial resolution of our observations does not allow us
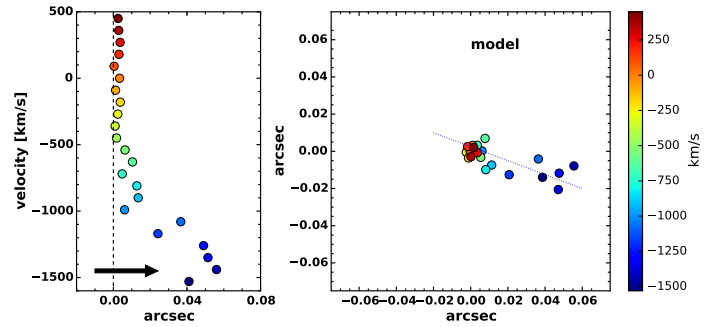
to discern whether our outflows are single explosive events or refilled with clouds ejected from the galactic disk. Hence, we assume a simple model where a single ionised cloud is ejected outward of the nuclear region and the mass outflow rate is equal to the mass of the outflow divided by the dynamical timescale (see eq. 1). The dynamic time is the time that a clump of ionised gas in outflow takes to reach a fixed distance from the QSO. We derive $\dot{M}_o$ values in the range $6 - 700$ M$_\odot$ yr^{-1}. We assume an average outflow mass rate error of $\pm$50%, which takes in account the uncertainties associated with the gas physical properties (i.e. density and temperature), flux calibrations and R_0 and v_0 estimates due to projection effects. For each source we estimate two value of $\dot{M}_o$ that are calculated by using Hβ and [OIII]λ5007 respectively. Since the [OIII]λ5007 outflow luminosities are $\sim$ 10 times larger than the ones from Hβ, the outflow masses inferred from the hydrogen emission line are $\sim$2 times larger than those estimated by [OIII]λ5007.

In Figure 9 we plot the outflow velocity and mass rate as a function of the AGN luminosity. L_{AGN} is derived by using the relation $L_{AGN} \sim 6\lambda L(\lambda 5100\text{Å})$ from Marconi et al. (2004). The solid and hollow blue points are the $\dot{M}_o$ estimated for five out of six QSOs; we could not infer the value of HE0251 since we were not able to measure the size of the outflow. The red points represent the ionised outflows observed in type 2 AGN at redshift $0.08 \lesssim z \lesssim 0.2$ (Harrison et al. 2014); the orange and purple points are from Brusa et al. (2015) and Cresci et al. (2015) who mapped ionised outflows in 6 X-ray selected, obscured QSOs at $z \sim 1.5$; the black circle corresponds to the the ionised outflow in a obscured radio-quiet QSO at $z \sim 0.123$ (Greene et al. 2012). For consistency with our work we re-calculated the outflows properties using an electronic density of $n_e = 500$ cm^{-3} and a temperature of $T_e = 10^4$ K. Note that the outflow masses from literature may be overestimated since we used the luminosities from the total [OIII]λ5007 and Hβ profiles.

In addition to ionised outflows, we compare our results with those obtained from molecular outflows (green, black and brown solid square; Cicone et al. 2014, Sun et al. 2014 and Feruglio et al. 2015, respectively). The molecular outflow properties were re-estimated assuming a shell-like cloud model (eq. 1).

In Figure 9 we show that the outflow velocity v_0 and outflow rate are correlated with the AGN luminosity, although with a large scatter. The increase in velocity and outflow rate with increasing AGN luminosity is consistent with the idea that a luminous AGN pushes away the surrounding gas through a radiatively driven fast wind whose kinetic power is a fraction of the AGN luminosity. However, it is not easy to establish a direct re-
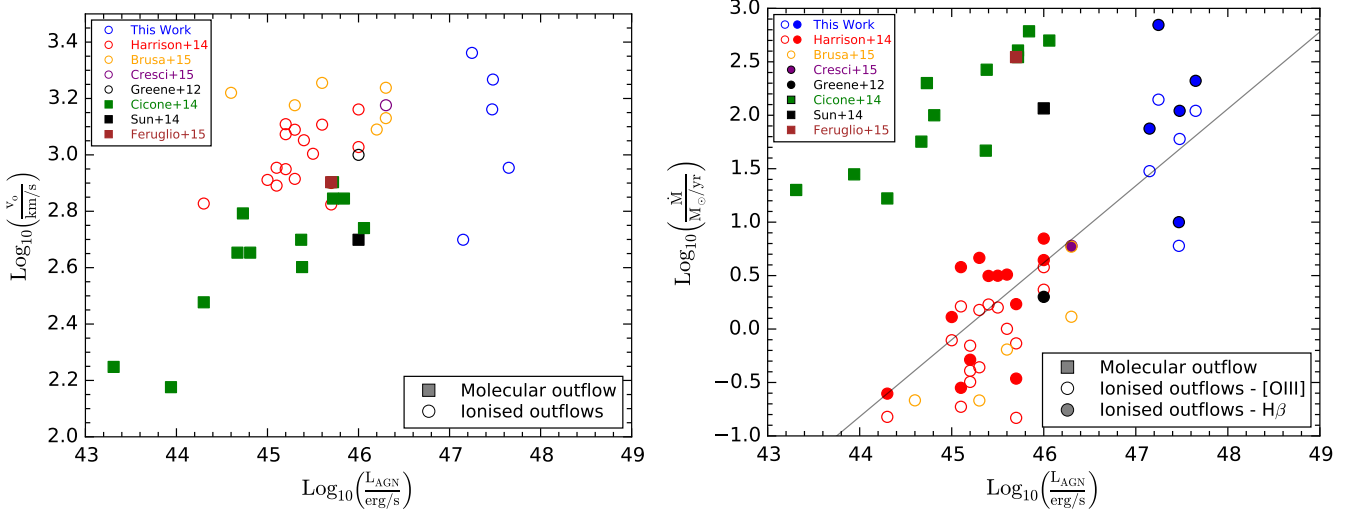
Fig. 9. Left : Outflow velocity as a function of the AGN bolometric luminosity. The blue circles denote the results from this work; the open circles mark the velocities of ionised gas (mainly [OIII]λ5007): the red, orange, purple and black circles are the estimates obtained from Harrison et al. (2014), Brusa et al. (2015), Cresci et al. (2015) and Greene et al. (2012), respectively. The green, black and brown squares denote the velocities of the molecular outflows from Cicone et al. (2014), Sun et al. (2014) and Feruglio et al. (2015). Right: Outflow rates as a function of the AGN bolometric luminosity. Notation is the same of the left panel expect that open circles mark the estimates obtained with [OIII]-inferred masses, while the filled ones denote the estimates based on Hβ. We recalculated the outflow properties inferred by previous works to make them consistent with our estimates (see text). The solid line is the best fit relation to the averages of filled and empty circles.

lation between AGN luminosity, velocity and outflow rate. The acceleration process of the outflow by the fast wind and the fraction of the kinetic power injected, might vary from object to object; moreover, the observed AGN luminosity may not represent the long-term average luminosity which is at the end responsible for driving the outflow. For these reasons we do not expect tight correlations between velocity, outflow rate and AGN luminosity, as observed. Indeed, previous studies on more heterogenous samples, but smaller luminosity ranges, did not find any significant correlation between the outflow velocities and the AGN luminosities (e.g. Veilleux et al. 2013, Brusa et al. 2015). In the luminosity range where we have data from both CO and [OIII] ($10^{44.5}$ erg/s $\lesssim L_{AGN} \lesssim 10^{46.5}$ erg/s), the velocities of the ionised outflows are a factor ~ 2 larger than those of the molecular gas, consistently with larger masses of molecular gas in both momentum- and energy-driven scenarios, but also with different acceleration/deceleration processes. However, given the heterogeneous nature of the sample and the non-uniform measurements of outflow velocities we cannot draw any firm conclusions. Moreover, there is only one galaxy (black circle and square in Fig. 9) where both molecular and ionised outflows are detected. This discrepancy is even more evident when comparing molecular with ionised outflow rates. Cicone et al. (2014) fit a a log-linear relation between $\dot{M}$ and L_{AGN} for their molecular outflows finding $Log_{10}(\dot{M}) = 2.84 + 0.720 \times Log_{10}(L_{AGN}/10^{46}erg/s)$ where we have corrected for the factor 3 discrepancy described in Section 5.1. Here, we fit the same relation between $\dot{M}$ and L_{AGN} fixing the slope to that of Cicone et al. (2014):

$$Log_{10}(\dot{M}) = (0.6 \pm 0.2) + 0.720 \times Log_{10}(L_{AGN}/10^{46}\text{erg/s}) \quad (10)$$

Since the velocities and the radii of ionised outflows are similar to those of molecular ones, we interpret the offset between the two L_{AGN}- $\dot{M}$ correlations as an indication that the ionised gas only traces a small fraction of the total gas mass. Comparing the normalization of the L_{AGN}- $\dot{M}$ relation inferred from our data with that obtained from molecular outflows, we can infer that the outflow rate of the ionised gas is a small fraction ($< 10\%$)
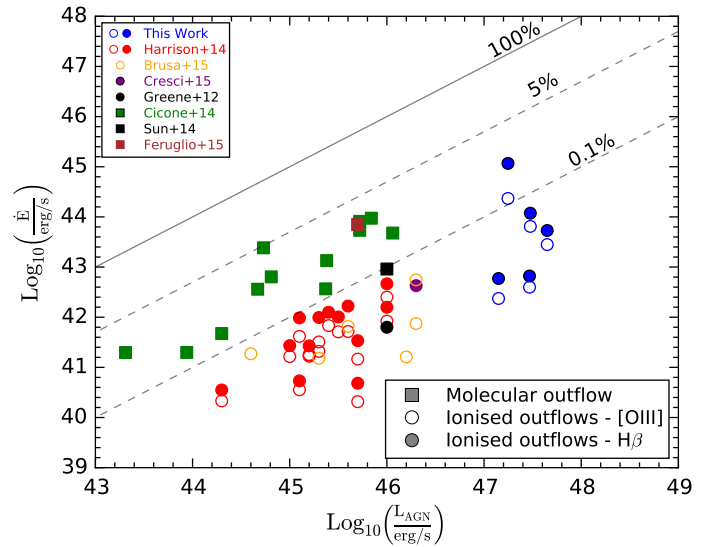

Fig. 10. Kinetic power as a function of the AGN bolometric luminosity. Symbols and colours as in fig. 9. The solid, dashed and dotted line correspond to $P_k = 100\%, 5\%, 0.1\%L_{AGN}$ respectively.

of the molecular one, suggesting that outflow masses are dominated by molecular gas. However, since molecular and ionised outflow rates are not estimated in the same objects and the relations have quite a large scatter, it is not possible to estimate the exact fraction of ionised gas in the outflows. On the other hand, the different normalisation could indicate that two different acceleration mechanisms are at work. Future ALMA observations of the molecular gas in these objects are essential to distinguish between these two different scenarios.

Figure 10 shows the kinetic power of outflowing gas as a function of AGN luminosity where the outflow kinetic energy rate is given by
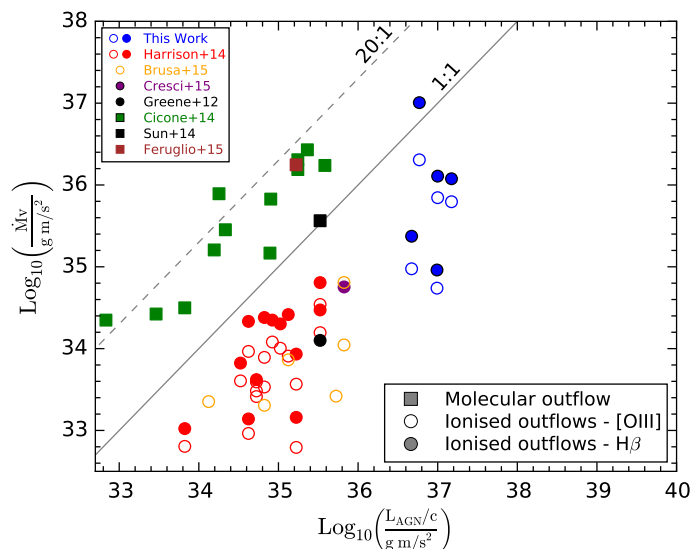
Fig. 11. Outflow momentum rate as a function of photon momentum of the AGN . Symbols and colours as in Fig. 9. The dotted and dashed line correspond to $\dot{P} \sim 20 L_{AGN}/$ c and $\dot{P} \sim L_{AGN}/$ c respectively.

$$\dot{E}_o = \frac{1}{2} \dot{M}_o v_o^2 = \frac{1}{2} \frac{M_o}{R_o} v_o^3$$

We indicate using solid, dashed and dotted lines the locus of points having an outflow kinetic power that is 100%, 5% and 0.1% of the AGN luminosity, respectively. The recent AGN feedback models (e.g. King 2010; Zubovas & King 2012; Lapi et al. 2014) predict a coupling efficiency between AGN-driven outflows and AGN power of about ~5% which is needed to explain the M_{BH} - σ relation observed in local galaxies. Although the molecular outflow observations are consistent with the models within the error, the kinematic power estimated from ionised outflows is only < 0.1% of the L_{AGN}. This percentage is too low to explain the M_{BH} - σ relation. Since the kinetic energy is proportional to the outflow mass, we cannot discern whether the nature of ionised outflows is different with respect to molecular ones or, as discussed above, the [OIII]λ5007 (and Hβ) line emission traces only a small fraction (< 10%) of the total outflowing gas.

The last fundamental parameter of the outflows is the outflow momentum rate defined as $v_o \dot{M}_o$. Energy-driven outflow models predict that the momentum of the large-scale outflow is boosted compared to the nuclear wind (or AGN radiation pressure momentum), i.e. $v_o \dot{M}_o \sim 20 L_{AGN}/$ c (Zubovas & King 2012). In Figure 11 we observe that molecular outflows follow the relation predicted by models (see Cicone et al. 2014 for more details) while ionised outflows are below the 1:1 relation. This could simply be the consequence of the discrepancy between the outflow masses of ionised and molecular gas.

Finally, we may conclude that the main difference between molecular and ionised outflows is the fraction of total gas mass pushed away from the AGN-driven wind. This is confirmed by the larger outflow rates (right panel of Fig. 9) and kinetic power (Fig. 10) of molecular outflows, and by their smaller outflow velocities (left panel of Fig. 9).

7. Conclusions

We performed seeing-limited, near-IR integral-field spectroscopic observations with SINFONI of a sample of six, high luminosity ($L_{bol} = 10^{13} - 10^{14}$ $L_\odot$) QSOs at redshift $z \sim 2.4$.

[OIII]λ5007 emission lines, redshifted into the H-band, are characterised by large FWHMs (> 1000 km/s) and prominent blue wings, indicative of fast outflows accelerated by the powerful AGN. We find that:

○ The [OIII]λ5007 emission line is spatially resolved in five out of six sources and extended over several kiloparsecs.

○ The analysis of the [OIII]λ5007 kinematical maps suggests the presence of conical outflows associated with regions of high velocity dispersions (> 500 km/s) The physical properties of the outflows, i.e. mass, outflow rate, kinetic energy and momentum rate, have been estimated with a new method based on spectroastrometry which is not affected by PSF smearing, at variance with results from previous works. The reliability of this method has been confirmed with a simple simulation but more accurate modelling will be developed in future work.

○ Both ionised and molecular outflow velocities are weakly correlated with the observed AGN luminosity, despite the large scatter, and at a given AGN luminosity the velocity of the ionised gas is roughly a factor 2 larger than that of the molecular one. However, given the heterogenous nature of the combined sample we cannot draw any firm conclusions.

○ Mass and momentum rates, as well as kinetic powers, increase with AGN bolometric luminosity in a similar way to what is observed in molecular outflows in the local universe. The ionised gas properties define relations with AGN luminosity which are parallel with those of molecular gas. In particular, ionised outflow rates are ~ 50 times lower than molecular ones. The kinetic power carried by ionised outflows is of the order of ~ 0.1 − 0.05% of the AGN luminosity compared to ~ 5% for molecular outflows. Finally, momentum rates are of the order of $L_{AGN}/$c, a factor ~ 20 − 50 smaller than for molecular outflows.

○ These discrepancies between ionised and molecular outflows can be explained with the fact that ionised gas traces a smaller fraction of the total gas mass. Alternatively, they are the indication of different acceleration mechanisms for the molecular and the ionised gas. Observations with ALMA would allow us to measure the molecular gas mass in these objects therefore distinguishing between these two scenarios.

References

Aalto, S., Garcia-Burillo, S., Muller, S., et al. 2015, A&A, 574, A85
Alexander, D. M., Swinbank, A. M., Smail, I., McDermid, R., & Nesvadba, N. P. H. 2010, MNRAS, 402, 2211
Bae, H.-J. & Woo, J.-H. 2014, ApJ, 795, 30
Baldry, I. K., Glazebrook, K., Brinkmann, J., et al. 2004, ApJ, 600, 681
Brusa, M., Bongiorno, A., Cresci, G., et al. 2015, MNRAS, 446, 2394
Cano-Díaz, M., Maiolino, R., Marconi, A., et al. 2012, A&A, 537, L8
Carniani, S., Marconi, A., Biggs, A., et al. 2013, A&A, 559, A29
Centeno, R. & Socas-Navarro, H. 2008, ApJ, 682, L61
Cicone, C., Feruglio, C., Maiolino, R., et al. 2012, A&A, 543, A99
Cicone, C., Maiolino, R., Gallerani, S., et al. 2015, A&A, 574, A14
Cicone, C., Maiolino, R., Sturm, E., et al. 2014, A&A, 562, A21

Costa, T., Sijacki, D., & Haehnelt, M. G. 2014, MNRAS, 444, 2355
Costa, T., Sijacki, D., & Haehnelt, M. G. 2015, MNRAS, 448, L30
Cresci, G., Mainieri, V., Brusa, M., et al. 2015, ApJ, 799, 82
Di Matteo, T., Springel, V., & Hernquist, L. 2005, Nature, 433, 604
Fabian, A. C. 2012, ARA&A, 50, 455
Faucher-Giguère, C.-A. & Quataert, E. 2012, MNRAS, 425, 605
Ferrarese, L. & Ford, H. 2005, Space Sci. Rev., 116, 523
Feruglio, C., Fiore, F., Carniani, S., et al. 2015, ArXiv e-prints [arXiv:1503.01481]
Feruglio, C., Fiore, F., Maiolino, R., et al. 2013a, A&A, 549, A51
Feruglio, C., Fiore, F., Piconcelli, E., et al. 2013b, A&A, 558, A87
Feruglio, C., Maiolino, R., Piconcelli, E., et al. 2010, A&A, 518, L155
Granato, G. L., De Zotti, G., Silva, L., Bressan, A., & Danese, L. 2004, ApJ, 600, 580
Greene, J. E., Zakamska, N. L., Ho, L. C., & Barth, A. J. 2011, ApJ, 732, 9
Greene, J. E., Zakamska, N. L., & Smith, P. S. 2012, ApJ, 746, 86
Harrison, C. M., Alexander, D. M., Mullaney, J. R., & Swinbank, A. M. 2014, ArXiv e-prints [arXiv:1403.3086]
Harrison, C. M., Alexander, D. M., Swinbank, A. M., et al. 2012, MNRAS, 426, 1073
Hopkins, P. F., Somerville, R. S., Hernquist, L., et al. 2006, ApJ, 652, 864
King, A. & Pounds, K. 2015, ArXiv e-prints [arXiv:1503.05206]
King, A. R. 2010, MNRAS, 402, 1516
Kormendy, J. & Ho, L. C. 2013, ARA&A, 51, 511
Lapi, A., Raimundo, S., Aversa, R., et al. 2014, ApJ, 782, 69
Liu, G., Zakamska, N. L., Greene, J. E., Nesvadba, N. P. H., & Liu, X. 2013, MNRAS, 436, 2576
Luridiana, V., Morisset, C., & Shaw, R. A. 2015, A&A, 573, A42
Madau, P. & Dickinson, M. 2014, ARA&A, 52, 415
Magorrian, J., Tremaine, S., Richstone, D., et al. 1998, AJ, 115, 2285
Maiolino, R., Gallerani, S., Neri, R., et al. 2012, MNRAS, 425, L66
Marconi, A. & Hunt, L. K. 2003, ApJ, 589, L21
Marconi, A., Risaliti, G., Gilli, R., et al. 2004, MNRAS, 351, 169
Markwardt, C. B. 2009, in Astronomical Society of the Pacific Conference Series, Vol. 411, Astronomical Data Analysis Software and Systems XVIII, ed. D. A. Bohlender, D. Durand, & P. Dowler, 251
Marziani, P., Sulentic, J. W., Stirpe, G. M., Zamfir, S., & Calvani, M. 2009, A&A, 495, 83
Menci, N., Fiore, F., Puccetti, S., & Cavaliere, A. 2008, ApJ, 686, 219
Nagao, T., Maiolino, R., & Marconi, A. 2006, A&A, 447, 863
Nayakshin, S. 2014, MNRAS, 437, 2404
Nesvadba, N. P. H., Polletta, M., Lehnert, M. D., et al. 2011, MNRAS, 415, 2359
Netzer, H., Shemmer, O., Maiolino, R., et al. 2004, ApJ, 614, 558
Pérez-González, P. G., Rieke, G. H., Villar, V., et al. 2008, ApJ, 675, 234
Perna, M., Brusa, M., Cresci, G., et al. 2015, A&A, 574, A82
Planck Collaboration, Ade, P. A. R., Aghanim, N., et al. 2014, A&A, 571, A16
Rodríguez Zaurín, J., Tadhunter, C. N., Rose, M., & Holt, J. 2013, MNRAS, 432, 138
Rodríguez Zaurín, J., Tadhunter, C. N., Rupke, D. S. N., et al. 2014, A&A, 571, A57
Rupke, D. S. N. & Veilleux, S. 2011, ApJ, 729, L27
Rupke, D. S. N. & Veilleux, S. 2013, ApJ, 775, L15
Shemmer, O., Netzer, H., Maiolino, R., et al. 2004, ApJ, 614, 547
Sun, A.-L., Greene, J. E., Zakamska, N. L., & Nesvadba, N. P. H. 2014, ApJ, 790, 160
Tombesi, F., Meléndez, M., Veilleux, S., et al. 2015, Nature, 519, 436
Tsuzuki, Y., Kawara, K., Yoshii, Y., et al. 2006, ApJ, 650, 57
van Dokkum, P. G. 2001, PASP, 113, 1420
Veilleux, S., Meléndez, M., Sturm, E., et al. 2013, ApJ, 776, 27
Zubovas, K. & King, A. 2012, ApJ, 745, L34
Zubovas, K. & King, A. R. 2014, MNRAS, 439, 400